

Supplementary information for:
**Intermediate photofragment distributions as probes of
non-adiabatic dynamics at conical intersections: Application to
the Hartley band of ozone**

David Picconi and Sergy Yu. Grebenshchikov^a

Department of Chemistry, Technische Universität München,

Lichtenbergstr. 4, 85747 Garching, Germany

^a Electronic mail: Sergy.Grebenshchikov@ch.tum.de

I. COMPUTATIONAL DETAILS

A. Propagation

The total and partial absorption cross sections are calculated using Eqs. (5), (6), and (8) of the main text, with the stationary energy component $\Psi^\lambda(\mathbf{Q}|E_{\text{ph}})$ expressed in terms of the Green's function,

$$\Psi^\lambda(\mathbf{Q}|E_{\text{ph}}) = \text{Im}G^+(E_{\text{ph}})\Phi_0 . \quad (1)$$

The advanced Green's function is constructed for the molecular Hamiltonian (Eq. (3) of the main text)

$$\hat{\mathbf{H}} = \hat{\mathbf{H}}^0 - iW\mathbf{1} . \quad (2)$$

augmented with a complex absorbing potential $-iW$ ($\text{Re}W > 0$),¹ approximately imposing the outgoing boundary conditions in the asymptotic region. Here $\mathbf{1}$ denotes the 2×2 identity matrix, and one coordinate function W is used in both electronic channels. The expression $\text{Im}G^+(E)\Phi_0(\mathbf{Q})$ is approximated by the expansion

$$\text{Im}G^+(E)\Phi_0(\mathbf{Q}) \simeq \sum_{n=0}^{N_{\text{iter}}} \text{Re}[b_n(E)]\Phi_n , \quad (3)$$

where $b_n(E)$ are the usual energy-dependent coefficients,² while the Krylov vectors Φ_n are found from a modified Chebyshev recursion relation due to Mandelshtam and Taylor.³ Chebyshev cross-correlation coefficients $x_{\gamma jv}^n = (\chi_{\gamma jv}|\Phi_n)$ are calculated for each Krylov vector, and the intermediate partial cross sections are reconstructed from $\{x_{\gamma jv}^n\}$ using the Eqs. (8), (15), (16) and (17) of the main text. The number of expansion terms, N_{iter} , is one of the convergence parameters of the calculation. The numerical parameters of the calculations are chosen as described in a previous paper:⁴ The Hamiltonian, Eq. (2), is set in discrete variable representation (DVR)⁵ with the grid comprising 200 potential-optimized⁶ points in $X \in [1.8, 10.0] a_0$, 140 potential-optimized points in $Y \in [1.8, 7.0] a_0$, and $N_Z = 80$ symmetry-adapted Gauss-Legendre quadrature points in angle. The grid is contracted by retaining only points with potential energy below $V_{\text{cut}} = 12.5$ eV above equilibrium in \tilde{X} . $N_{\text{iter}} = 25\,000$ Chebyshev iterations are sufficient to converge the absorption spectrum and the partial cross sections. The complex absorbing potential $-iW$ is set via a coordinate dependent damping function $\gamma(Q)$ ($Q = X$ or Y) as described in Refs. 3, 7, and 8. It

becomes non-zero in a $1.0 a_0$ -wide strip at the grid edge, grows quadratically as a function of O/O₂ distance inside the strip, and reaches the strength of 0.10 at the grid edge.

B. Basis functions for the calculation of Raman amplitudes

The vibrational basis states $\{\phi_k(\mathbf{Q})\}$ have been calculated using the potential energy surface (PES) of the ground electronic state constructed in Ref. 9. The potential is based on the global PES of Siebert *et al.*^{10,11} subsequently refined in Refs. 12 and 13. The employed PES includes only one deep potential well of one stable O₃ conformer. The van der Waals wells in the asymptotic regions, giving rise to a dense spectrum of van der Waals vibrational levels near the dissociation threshold,^{14,15} are eliminated.

With the chosen PES, all vibrational states for non-rotating ozone ⁴⁸O₃ were calculated up to dissociation threshold using settings similar to those described in Ref. 9. The ozone Hamiltonian $\hat{H}_{\hat{X}}$ was set in DVR and diagonalized in a set of narrow energy windows using Filter Diagonalization.¹⁶ The number of Chebyshev iterations used to construct the energy-adapted basis³ was 200 000. Jacobi coordinates (X', Y', Z') , used in the calculation, are different from the ones described in Sect. 2 of the main text: X' is the distance from the central atom to the center of mass of the two end atoms, Y' is the distance between the two end atoms, and Z' is the angle between \mathbf{X}' and \mathbf{Y}' . The grid in X' and Y' ranged from $0.1 a_0$ to $6 a_0$ and from $1.7 a_0$ to $8 a_0$, respectively; for both coordinates 78 potential optimized⁶ DVR points were used. The angular grid comprised 70 symmetry reduced Gauss-Legendre grid points in the interval $(0^\circ, 90^\circ)$; all calculated eigenstates were either symmetric or antisymmetric with respect to the interchange of the two end atoms, $Z' \rightarrow \pi - Z'$. The grid points with potential energies over 2 eV above classical dissociation threshold were discarded. A total of 244 states (138 symmetric and 106 antisymmetric states) were found.

II. VIBRATIONALLY ADIABATIC BASIS STATES AT INTERMEDIATE INTERFRAGMENT DISTANCES

This section illustrates the calculation of vibrationally adiabatic eigenstates at intermediate interfragment distances, in terms of which the intermediate distributions $P_\gamma(j, v)$ are defined.

For a given fixed dissociation coordinate X_* the local Hamiltonians $\mathcal{H}_\gamma(Y, Z|X_*)$ for the diabatic states $\gamma = \text{B}$ or R read as

$$\mathcal{H}_\gamma(Y, Z|X_*) = -\frac{1}{2\mu_Y} \frac{\partial^2}{\partial Y^2} - \left(\frac{1}{\mu_X X_*^2} + \frac{1}{\mu_Y Y^2} \right) \frac{1}{\sin Z} \frac{\partial}{\partial Z} \sin Z \frac{\partial}{\partial Z} + V_\gamma(X_*, Y, Z) . \quad (4)$$

Here, μ_X and μ_Y are the reduced masses of O_2 and $\text{O} - \text{O}_2$, respectively. These two-dimensional Hamiltonians are not separable for two reasons: first, the potentials $V_\gamma(X_*, Y, Z)$ couple the coordinates Y and Z ; second, the angular kinetic energy operator also couples Y and Z .

The local basis in each diabatic electronic state is defined in terms of a separable approximate Hamiltonian with the eigenstates factorized into an X - and Y -dependent terms, and the eigenenergies given by a sum of vibrational and rotational energies. The eigenstates can be assigned the rovibrational quantum numbers (j, v) automatically, so that a visual inspection of the two dimensional wave functions can be dispensed with. Using the separable Hamiltonian for each diabatic electronic state, the total energy is separated into individual local vibrational (stretching and bending) and translational contributions. Another advantage of the separable approximation is that it allows one to localize the projection basis in a single arrangement channel for arbitrary interfragment distances.

The following approximate separable Hamiltonian is used to define the local adiabatic projection states for a given X_* :

$$\mathcal{H}_\gamma^{\text{Sep}}(X_*) = -\frac{1}{2\mu_Y} \frac{\partial^2}{\partial Y^2} + V_\gamma(X_*, Y, Z_{\gamma, \text{min}}) \quad (5a)$$

$$- \left(\frac{1}{\mu_X X_*^2} + \frac{1}{\mu_Y Y_{\gamma, \text{min}}^2} \right) \frac{1}{\sin Z} \frac{\partial}{\partial Z} \sin Z \frac{\partial}{\partial Z} + V_\gamma(X_*, Y_{\gamma, \text{min}}, Z) \quad (5b)$$

$$- V_{\gamma, \text{min}}(X_*) .$$

Here $V_{\gamma, \text{min}} = V_\gamma(X_*, Y_{\gamma, \text{min}}, Z_{\gamma, \text{min}})$ is the minimum of the two-dimensional potential $V_\gamma(X_*, Y, Z)$, with the coordinates $\{Y_{\gamma, \text{min}}, Z_{\gamma, \text{min}}\}$. The term (5a) acts only on Y , the term (5b) acts only on Z , and the Hamiltonian is separable. The eigenfunctions are in the product form $\chi_{\gamma j v}(Y, Z) = F_{\gamma v}(Y)G_{\gamma j}(Z)$ and the respective energies are $\epsilon_{\gamma j v} = V_{\gamma, \text{min}} + \epsilon_{\gamma v} + \epsilon_{\gamma j}$. Eigenfunctions and eigenenergies obey the following one-dimensional equations,

$$\left[-\frac{1}{2\mu_Y} \frac{\partial^2}{\partial Y^2} + V_\gamma(X_*, Y, Z_{\gamma, \text{min}}) \right] F_{\gamma v}(Y) = (V_{\gamma, \text{min}} + \epsilon_{\gamma v}) F_{\gamma v}(Y) \quad (6)$$

and

$$\left[- \left(\frac{1}{\mu_X X_\star^2} + \frac{1}{\mu_Y Y_{\gamma,\min}^2} \right) \frac{1}{\sin Z} \frac{\partial}{\partial Z} \sin Z \frac{\partial}{\partial Z} + V_\gamma(X_\star, Y_{\gamma,\min}, Z) \right] G_{\gamma j}(Z) = (V_{\gamma,\min} + \epsilon_{\gamma j}) G_{\gamma j}(Z). \quad (7)$$

In Eq. (7) the angular kinetic energy operators is uncoupled to the coordinate Y . Therefore the approximate separable Hamiltonian (20) differs from the exact Hamiltonian (4) also for $X \rightarrow \infty$, since it neglects the centrifugal distortion. We checked that this approximation produced little changes in the final rotational distributions, and negligible variations in the final vibrational distributions.

The DVR grid points in X taken from the three-dimensional Chebyshev propagation of Sect. I, have been used as X_\star in Eqs. (6) and (7). Equation (6) has been first solved on a dense evenly spaced DVR grid of 400 points; next, the calculated eigenfunctions have been interpolated to the DVR grid points in Y used in the 3D propagation. Equation (7) has been solved directly on the Legendre DVR grid used in the 3D propagation.

The separable energies and wavefunctions are good approximations to the eigenenergies and the wave functions of the 2D Hamiltonian (4), both in the asymptotic region (where the fragment wavefunctions have the exact product form) and in the inner part of the potentials. Figs. S1 and S2 compare the exact two-dimensional potential energy surfaces with the approximate separable potential energy surfaces at two interfragment distances X_\star and demonstrates the quality of the separable approximation.

The partial cross-sections can be calculated with two methods, both implemented in our codes. The first option is to pre-select a set of distances X_\star , to calculate the vibrationally adiabatic eigenfunctions using Eqs. (6) and (7), and to compute the Chebyshev cross-correlation coefficients $\{x_{\gamma jv}^n\}$. With this method, the distributions at a given X_\star can be evaluated for an arbitrary photon energy.

The second option is to evaluate the partial cross sections for a given E_{ph} using the fixed energy component $\Psi^\lambda(\mathbf{Q}|E_{\text{ph}})$. This method allows one to compare different definitions, Eqs. (16) and (17) of the main text, of the T -matrix elements at intermediate X_\star . The functions $f_{\gamma jv}$ are the projections $\langle \Psi_\gamma^\lambda(X, Y, Z) | \delta(X - X_\star) | \chi_{\gamma jv}(Y, Z | X_\star) \rangle$, for which the numerical derivatives required in Eqs. (14) and (17) of the main text, are easily evaluated using the DVR representation of the operator $\partial/\partial X$.

The differences between the distributions obtained with Eqs. (16) and (17) of the main

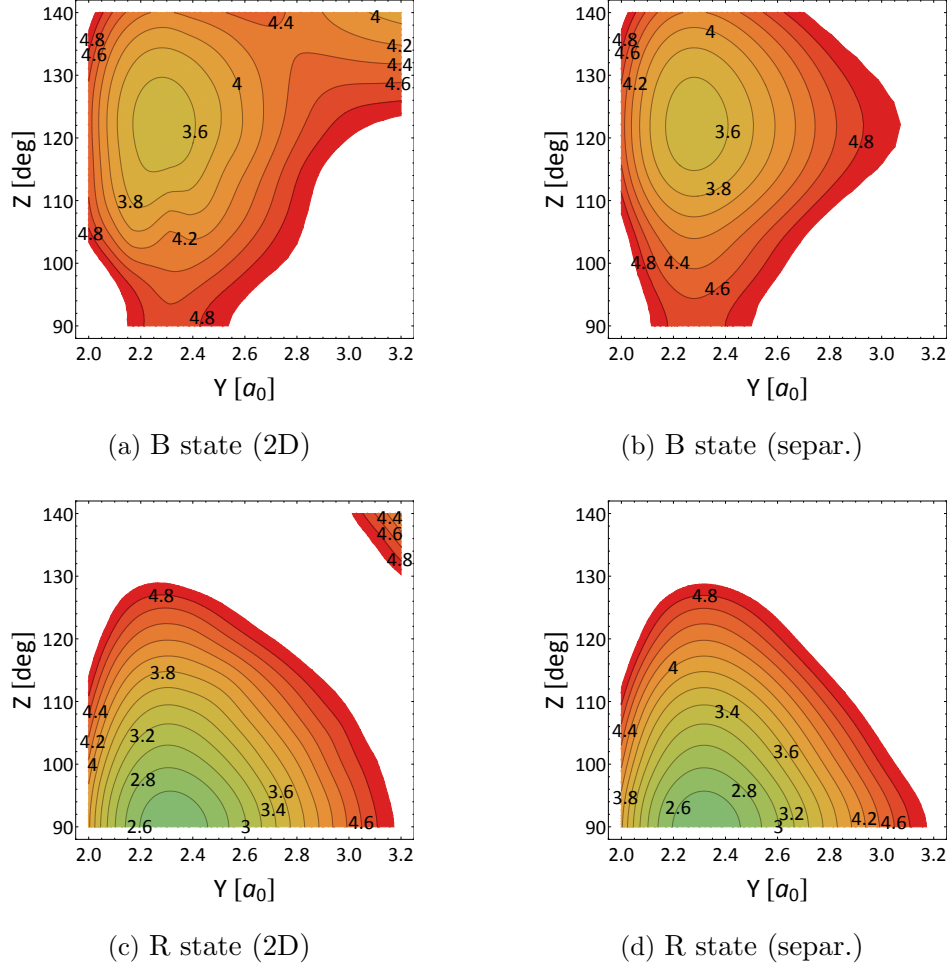


FIG. S1. Comparison between the exact 2D surfaces (left) and the surfaces used in the separable approximation (right) for the states B (top) and R (bottom), plotted in the (Y, Z) plane at the dissociation distance $X_\star = 3.56 a_0$. Contour energies in each frame are given in eV, relative to the minimum of the ground electronic state \tilde{X} .

text are illustrated in Fig. S3 for two interfragment distances X_\star . The differences are immaterial for large X_\star , and remain negligibly small in the interaction region, too.

A. Comparison between the exact and the ‘separable’ intermediate eigenenergies

In this Section, the spectrum of the approximate separable Hamiltonian, Eq. (20), is compared with the spectrum of the full adiabatic Hamiltonian, Eq. (4). To this end, the 2D Hamiltonian, Eq. (4), for a given distance X_\star has been set in the basis of the separable

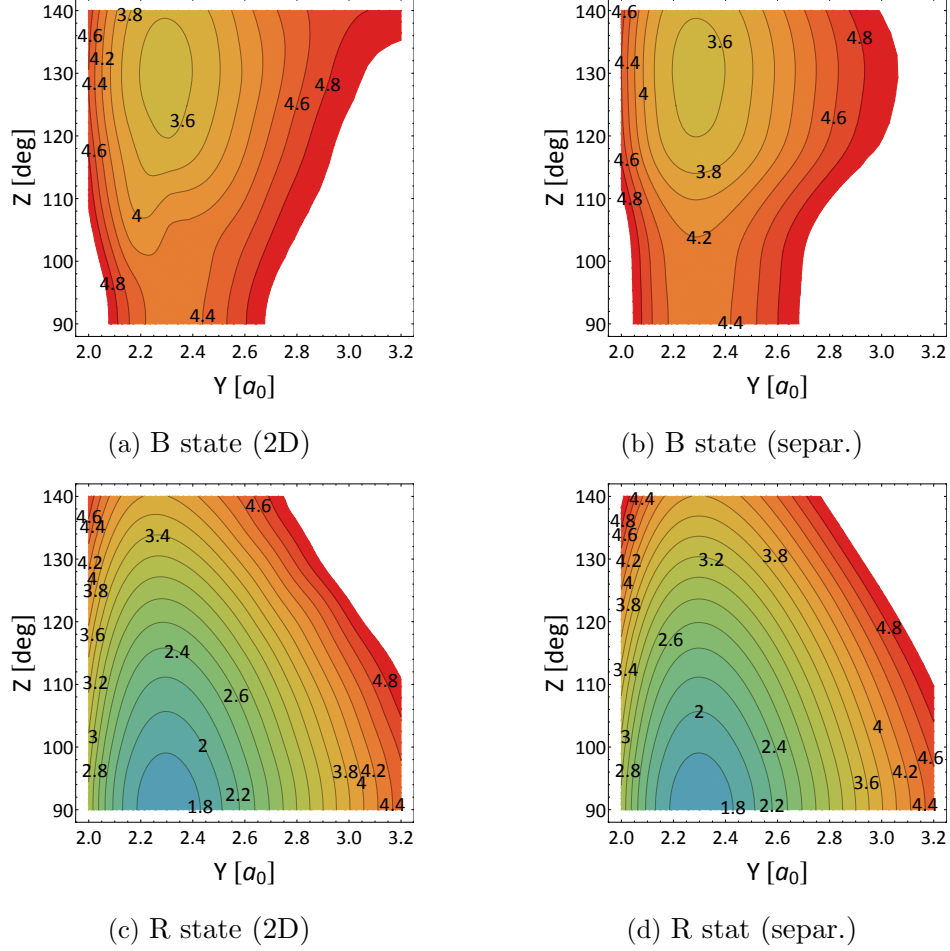


FIG. S2. The same as in Fig. S1, but for the interfragment distance of $X_\star = 4.00 a_0$.

wave functions $\{\chi_{\gamma jv}(Y, Z)\}$ described above, and the matrix

$$H_{jv, j'v'}^{(2D, \gamma)} = \langle F_{\gamma v}(r)G_{\gamma j}(\theta) | \mathcal{H}_\gamma(r, \theta; R_\star) | F_{\gamma v'}(r)G_{\gamma j'}(\theta) \rangle \quad (8)$$

has been diagonalized. Only wave functions with energies below a threshold energy E_{thr} are included. E_{thr} is a parameter of the calculation.

Thus, the two dimensional wave functions at intermediate distances are found as linear combinations of separable eigenstates,

$$\psi_{\gamma k}^{2D}(Y, Z) = \sum_{jv} C_{\gamma k, jv} F_{\gamma v}(Y) G_{\gamma j}(Z) . \quad (9)$$

For many 2D eigenstates this expression allows one to find a unique separable counterpart, with a single leading coefficient such that $|C_{\text{max}}|^2 > 0.5$. In these cases the energy levels of the two Hamiltonians can be directly compared. In Fig. S4 the difference between the exact energy and the energy of the corresponding separable eigenstate ($\Delta E_{\gamma jv}$) is plotted against

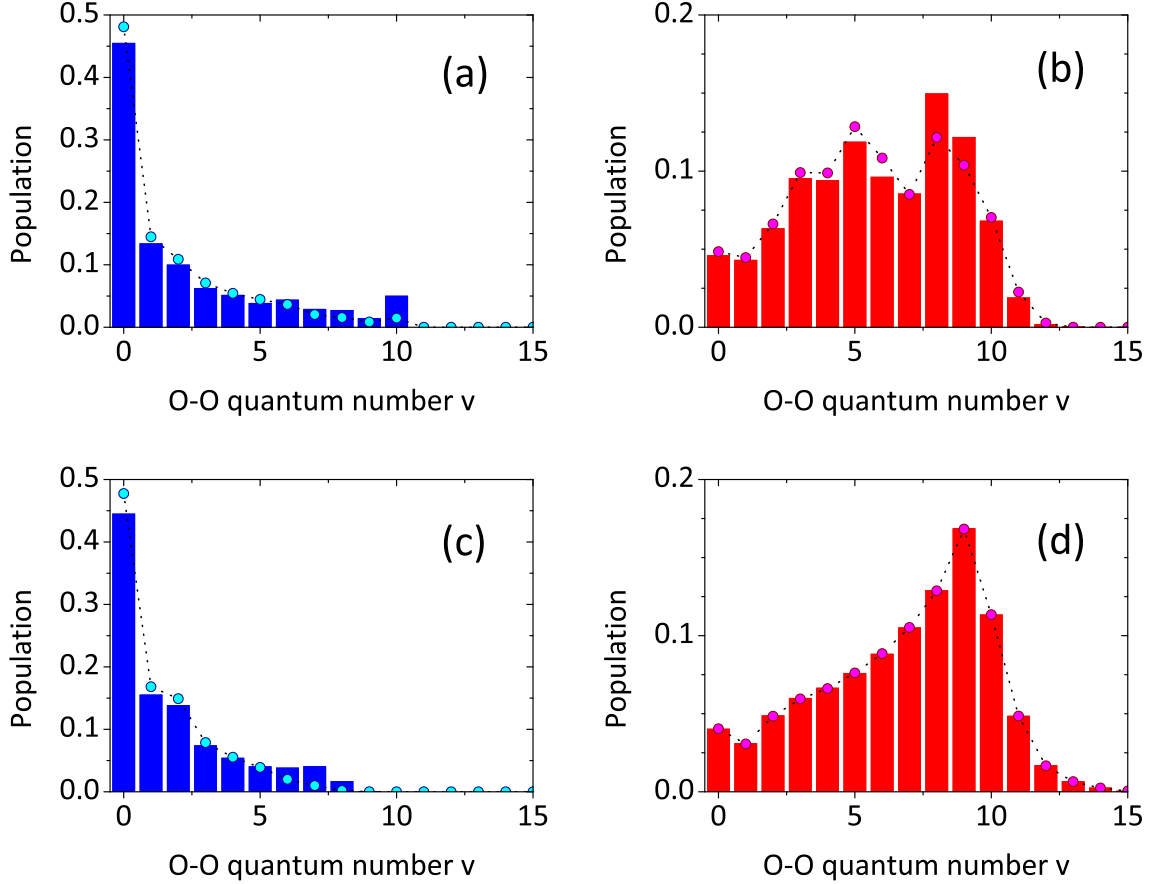


FIG. S3. Comparison between the vibrational populations calculated using Eqs. (16) (histograms) and (17) (connected dots) of the main text, for $\lambda = 250$ nm. (a): B state, $X_{\star} = 3.82 a_0$; (b): R state, $X_{\star} = 3.82 a_0$; (c): B state, $X_{\star} = 4.32 a_0$; (d): R state, $X_{\star} = 4.32 a_0$.

the exact eigenenergy for $X_{\star} = 3.78 a_0$. For most vibrational states in either B or R, the differences are less than 0.04 eV, suggesting that the separable approximation is reliable also near the conical intersection.

Additionally, we calculated the average absolute difference between the energies of the separable and the exact two-dimensional model, with the populations of the intermediate eigenstates taken into account:

$$\langle \Delta E_{\gamma}(E_{\text{ph}}) \rangle = \frac{\sum_{jv} |\Delta E_{\gamma jv}| P_{\gamma}(j, v | E_{\text{ph}})}{\sum_{jv} P_{\gamma}(j, v | E_{\text{ph}})}. \quad (10)$$

The sums include only the eigenstates with $|C_{\text{max}}|^2 > 0.5$, assigned to particular quantum numbers (j, v) . The average differences $\langle \Delta E_{\text{B}} \rangle$ and $\langle \Delta E_{\text{R}} \rangle$ are shown in Fig. S5 against the photon energy, which enters Eq. (10) through the E_{ph} dependent intermediate populations.

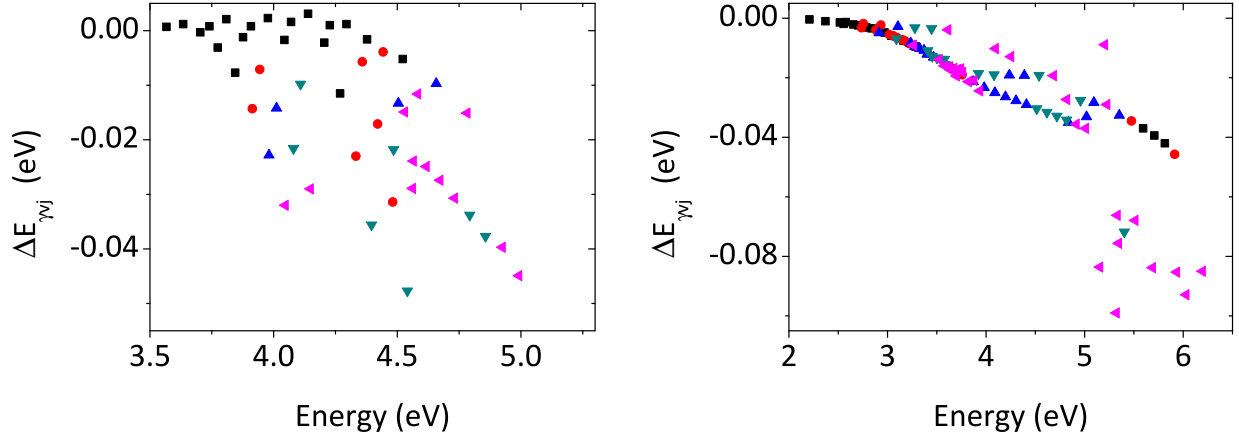


FIG. S4. Difference between the energies of the exact two-dimensional Hamiltonian and the approximate separable one, plotted against the energy. The intermediate distance is $X_* = 3.78 a_0$. The left (right) panel shows the eigenenergies of the B (R) state. The dots have different colors according to the value of the maximum absolute square of the coefficient in the expansion (9), namely black for $|C_{\max}|^2 > 0.9$, red for $0.8 < |C_{\max}|^2 \leq 0.9$, blue for $0.7 < |C_{\max}|^2 \leq 0.8$, green for $0.6 < |C_{\max}|^2 \leq 0.7$ and magenta for $0.5 < |C_{\max}|^2 \leq 0.6$. The two-dimensional eigenstates with large $|C_{\max}|^2$ are better reproduced by the approximate separable eigenstates.

Although the differences $\Delta E_{B,R}$ increase with the photon energy, they remain below 0.025 eV.

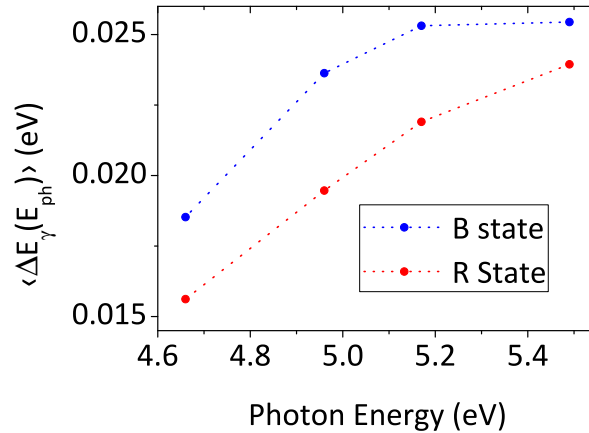


FIG. S5. Average absolute difference between the exact (2D) and the separable energies of the intermediate eigenstates ($X_* = 3.78 a_0$), Eq. (10), plotted against the photon energy, for the B and the R states.

III. RELATIVE ELECTRONIC POPULATIONS VERSUS THE INTERFRAGMENT DISTANCE X

The intermediate distributions in the main text are constructed for interfragment distances X_* located in the vicinity of the conical intersection between the states B and R. The distances, defining this ‘vicinity’, can be found, for example, by following the population of the initially empty R state as a function of X : Significant population transfer into the R state at a certain X signals that one has reached a dynamically significant B/R crossing region. The relative population

$$\frac{\langle \Psi_R^\lambda | \delta(X - X_*) | \Psi_R^\lambda \rangle}{\sum_{\gamma=B,R} \langle \Psi_\gamma^\lambda | \delta(X - X_*) | \Psi_\gamma^\lambda \rangle}$$

of the R state is plotted in Fig. S6 as a function of X .

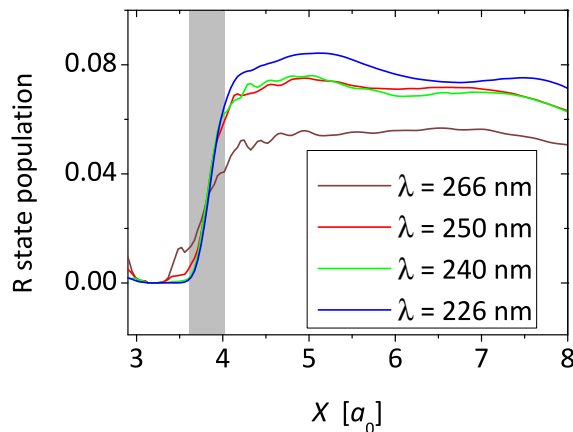


FIG. S6. Population of the R state as a function of the interfragment distance for four different photon wavelengths. The gray strip highlights the region of the conical intersection, and it is centered at the distance of the minimum of the crossing seam.

Since only the B state is initially excited, the population is close to zero for the O—O₂ distances smaller than $3.5 a_0$. The asymptotic value is reached for $R > 4.5 a_0$; most of the population transfer occurs in the shaded region between $3.75 a_0$ and $4.0 a_0$, where the conical intersection is located. The asymptotic quantum yield for the R channel increases with increasing photon energy and ranges between 5% (at $\lambda = 266$ nm) and 8% (at $\lambda = 226$ nm).

IV. LANDAU-ZENER RECONSTRUCTION OF THE INTERMEDIATE VIBRATIONAL DISTRIBUTIONS FOR DIFFERENT PHOTON ENERGIES

Figure S7 shows the intermediate O – O vibrational distributions in the R state, calculated using the Landau-Zener model (Eq. (21) of the main text), compared to the quantum mechanical distributions obtained directly from T -matrix elements. The distributions for $E_{\text{ph}} = 5.49$ eV are shown in Fig. 2(b) of the main text; Fig. S7 shows the results for several other photon energies. The extension of the distributions toward high v with increasing E_{ph} is perfectly reproduced by the Landau-Zener model. The accuracy of the model is the highest for large photon energies and somewhat decreases for decreasing E_{ph} .

The quality of the state-averaged LZ model presented in Fig. S7 is influenced by the differences between the vibrationally adiabatic eigenstates in the electronic states B and R. Indeed, Eqs. (23) and (24) of the main text describe the internal conversion as a ‘jump’ from the rovibronic state (B, j, v) to the rovibronic state (R, j, v) with a Landau-Zener probability w_{jv}^{LZ} . It is explicitly assumed that the vibrational quantum numbers (j, v) do not change as the molecule undergoes an electronic transition and, moreover, the vibrational wave functions in both electronic states are identical. This assumption is valid, by definition, at every point along the crossing seam. However, it can be violated if X_{\star} is chosen in a broad vicinity of the crossing, where the two states are not strictly degenerate. In this case, the validity of the simple state-averaged Landau-Zener model strongly depends on how similar the potentials and the vibrational eigenstates of the B and R states in the (Y, Z) plane are. Suppose for example that in the crossing region the minima of the potentials $V_{\text{B}}(X_{\star}, Y, Z)$ and $V_{\text{R}}(X_{\star}, Y, Z)$ lie in two different regions of the (Y, Z) plane. The vibrational wave functions in B and R are localized in the respective regions and only partially overlap, and the Gaussian of the $(B, 0, 0)$ state is shifted relative to the Gaussian of the $(R, 0, 0)$ state. In the state-averaged Landau-Zener model the transition probability between these two states is given by the Massey parameter ξ_{00} evaluated using only one of the two Gaussians. The second Gaussian and the overlap of the two functions are ignored.

In the vicinity of the B/R crossing, the equilibrium O—O distance is essentially the same for the states B and R. In contrast, the minimum along the angle Z in the R state is displaced relative to the B state by nearly 30° (see Figs. S1 and S2). The impact, which this angular displacement has on the state-averaged LZ model, is illustrated in Fig. S8, which compares

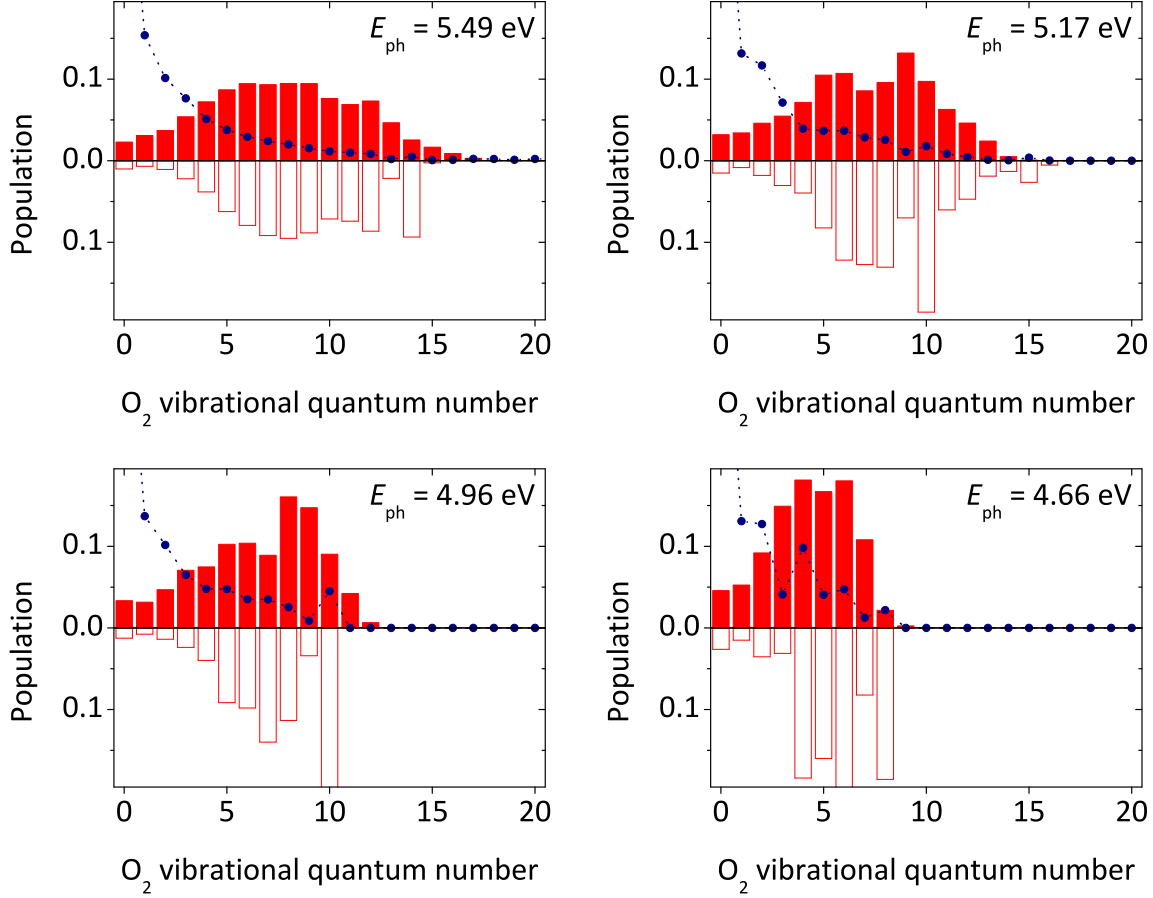


FIG. S7. Normalized quantum mechanical vibrational distributions in the short O—O bond stretch in the R state evaluated at $X_\star = 3.90 a_0$, for different photon energies (filled histograms). The same distributions reconstructed using the state-averaged Landau-Zener model are shown with empty histograms. The blue dots indicate the B state distribution $P_B(j, v)$ at $X_\star = 3.90 a_0$, used in Eq. (22) of the main text as incident distribution (the population for $v = 0$ is out of scale).

in the (j, v) plane the quantum mechanical intermediate distribution in the R state, $P_R(j, v)$, with the distribution $P_R^{LZ}(j, v)$ reconstructed from the incident distribution $P_B(j, v)$ via

$$P_R^{LZ}(j, v) = P_B(j, v) w_{jv}^{LZ}(\text{B} \rightarrow \text{R}) . \quad (11)$$

Each (j, v) state is represented by a dot whose color varies from yellow (unpopulated state), through green (low population) and light blue (medium population) to dark blue (large population). Only open intermediate channels are shown in Fig. S8.

Only a relatively small fraction of the allowed channels is appreciably populated in the R state, and the corresponding black dots trace a nearly straight line passing between

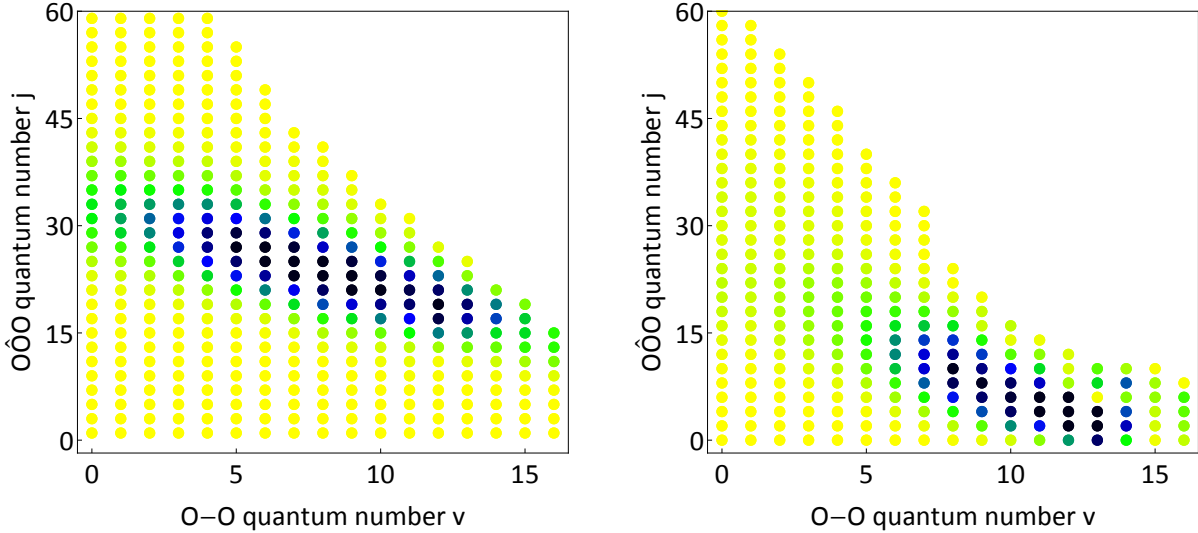


FIG. S8. Intermediate (j, v) distributions for a photon energy $E_{\text{ph}} = 5.49$ eV. (a) Population calculated using the quantum mechanical T -matrix elements, $P_{\text{R}}(j, v)$, at $X_{\star} = 3.90 a_0$; (b) Population $P_{\text{R}}^{\text{LZ}}(j, v)$ calculated using the ‘diagonal’ Landau-Zener model described in the main text. Yellow color corresponds to $P(j, v) < 0.002$, green to $0.002 < P(j, v) < 0.007$, blue to $0.007 < P(j, v) < 0.018$, black to $P(j, v) > 0.018$.

($v = 5, j = 28$) and ($v = 12, j = 20$). The state-average LZ model correctly reproduces the O—O vibrational distribution along the v -axis. In contrast, the population maximum along the j -axis is shifted in $P_{\text{R}}^{\text{LZ}}(j, v)$ to lower j values. The formal reason for this is the shape of the incident distribution $P_{\text{B}}(j, v)$: While the populated v -levels in the B state span the range $0 \leq v \leq 15$, the population of states with the bending quantum number $j > 20$ is very low. As a result, these states are missing in the distribution P_{R}^{LZ} , reconstructed using the state-averaged LZ model. Because the potential minimum along the bending mode Z is displaced in the R state to smaller angles relative to the B state, the vibrational states (B, j, v) with low $j < 20$ are expected to have substantial projection coefficients onto the bending states (R, j, v) with $j > 20$. In other words, the B/R transitions in the basis of the two vibrational manifolds are non-diagonal. The ‘diagonal’ state-averaged Landau-Zener model takes into account only the individual probability of transfer from the state (B, j, v) , and not the redistribution of the population in the manifold of (R, j, v) states.

A ‘non-diagonal’ extension of Eq. (11), where also the rovibrational levels of the R states are considered, requires a solution of a multistate Landau-Zener problem, with all diabatic coupling matrix elements $\langle \chi_{\text{R}j'v'}(Y, Z|X_{\star}) | V_{\text{BR}}(X_{\star}, Y, Z) | \chi_{\text{B}jv}(Y, Z|X_{\star}) \rangle$ taken into account.

A rigorous approach can be based on a detailed semiclassical analysis of the close coupling equations set in the appropriate vibronic basis.¹⁷⁻²¹ This extension lies beyond the scope of the present study, in which the non-adiabatic problem is solved fully quantum mechanically, and will be discussed elsewhere. The attractive feature of the approximate ‘diagonal’ approximation is that it leads to a practically useful relation $\xi_{\text{eff}} = -\ln(1 - P_R(v)/P_B(v))$ used in the main text to reconstruct the v -dependence of the Massey parameter from the intermediate vibrational distributions (see discussion after Eq. (23) of the main text).

V. RAMAN WAVE FUNCTIONS

The Raman wave functions in both electronic channels γ are shown in Fig. S9 in Jacobi coordinates (X, Y) for the incident photon energies $E_{\text{ph}} = 4.96 \text{ eV}$ and $E_{\text{ph}} = 5.49 \text{ eV}$ (corresponding to the photolysis wavelengths of $\lambda_{\text{I}} = 250 \text{ nm}$ and $\lambda_{\text{I}} = 226 \text{ nm}$). They are filtered out of the initial wave packet Φ_0 according to Eq. 6 of the main text (see also Ref. 4).

The Raman wave functions provide a detailed illustration of the mechanism by which the coupling mode Y becomes excited along the adiabatic path. Indeed, the probability maxima in the asymptotic channels of both electronic states trace out clearly visible short-bond oscillations resembling the familiar quasi-classical trajectories for vibrationally excited products. In the optically bright B state, the oscillations have small amplitude and are caused not so much by the passage through the intersection (which has no visible effect on the wave function) as by a slight difference in the equilibrium bond lengths in the parent molecule and the O_2 fragment. In the R state, the molecules emerge in the intersection region with a visibly stretched O_2 bond, and this quantum mechanical over-stretching of the coupling mode is the ‘mechanistic’ origin of the inverted vibrational distributions created upon the adiabatic passage through the conical intersection.

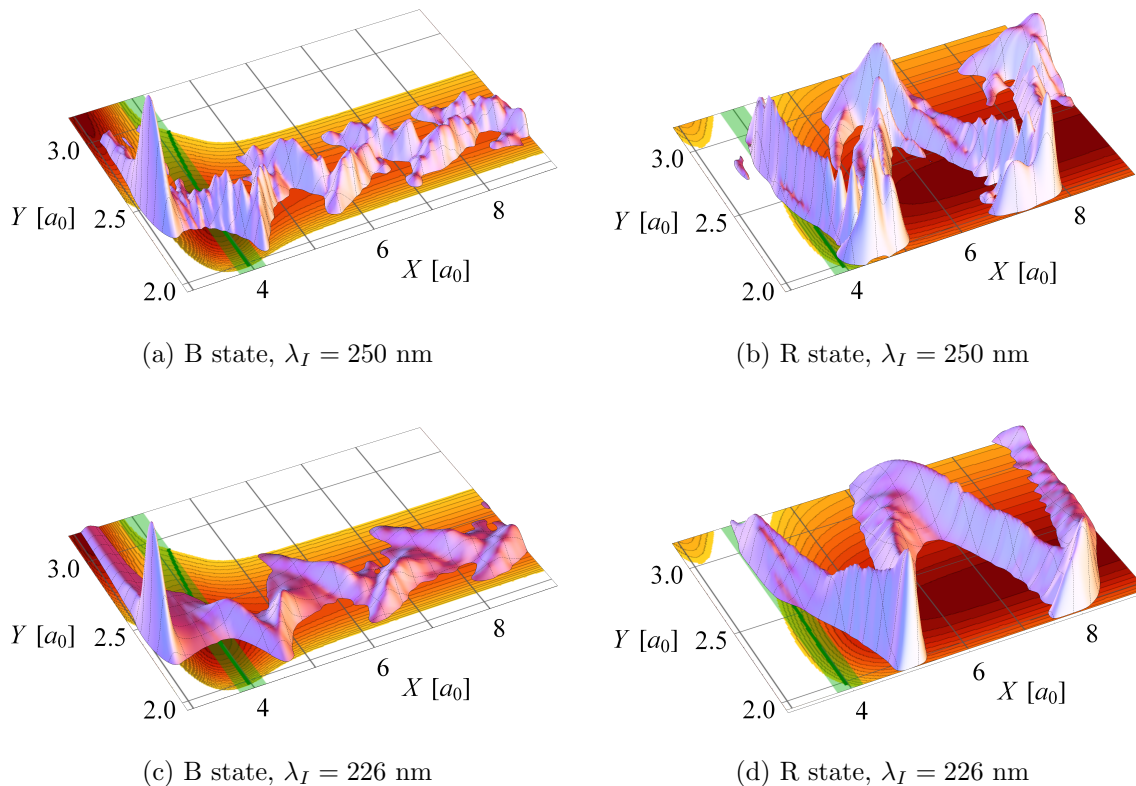


FIG. S9. Electronic components of the Raman wavefunctions in the B state (left panels) and in the R state (right panels) for $\lambda_I = 250$ nm (top) and $\lambda_I = 226$ nm (bottom), corresponding to photon energies of $E_{\text{ph}} = 4.96$ eV and $E_{\text{ph}} = 5.49$ eV, respectively. The probability distributions $|\Psi_\gamma^\lambda|^2$, integrated over the angle Z , are shown as 3D plots in the (X, Y) plane. In each panel, the contour maps of the diabatic B and R potentials taken at $Z = 134^\circ$ are plotted in the (X, Y) plane. The shaded green strip highlights the B/R intersection region, and the crossing seam is marked with a tick line.

¹ G. Jolicard and E. J. Austin. *Chem. Phys. Lett.*, 121:106, 1985.

² H. Tal-Ezer and R. Kosloff. *J. Chem. Phys.*, 81:3967, 1984.

³ V. A. Mandelshtam and H. S. Taylor. *J. Chem. Phys.*, 103:2903, 1995.

⁴ D. Picconi and S. Yu. Grebenshchikov. *J. Chem. Phys.*, 141:074311, 2014.

⁵ J. C. Light and T. Carrington. *Adv. Chem. Phys.*, 114:263, 2000.

⁶ J. Echave and D. C. Clary. *Chem. Phys. Lett.*, 190:225, 1992.

⁷ V. A. Mandelshtam and H. S. Taylor. *J. Chem. Soc. Faraday Trans.*, 93:847, 1997.

- ⁸ B. Kirmse, B. Abel, D. Schwarze, S. Yu. Grebenshchikov, and R. Schinke. *J. Phys. Chem. A*, 104, 2000.
- ⁹ M. Ivanov, S. Yu. Grebenshchikov, and R. Schinke. *J. Chem. Phys.*, 120:10015, 2004.
- ¹⁰ R. Siebert, R. Schinke, and M. Bittererova. *Phys. Chem. Chem. Phys.*, 3:1795, 2001.
- ¹¹ R. Siebert, P. Fleurat-Lessard, R. Schinke, M. Bittererova, and S. C. Farantos. *J. Chem. Phys.*, 116:9749, 2002.
- ¹² P. Fleurat-Lesard, S. Yu. Grebenshchikov, R. Siebert, R. Schinke, and N. Halberstadt. *J. Chem. Phys.*, 118:610, 2003.
- ¹³ D. Babikov, B. K. Kendrick, R. B. Walker, R. T. Pack, P. Fleurat-Lessard, and R. Schinke. *J. Chem. Phys.*, 118:6298, 2003.
- ¹⁴ S. Yu. Grebenshchikov, R. Schinke, P. Fleurat-Lessard, and M. Joyeux. *J. Chem. Phys.*, 119:6512, 2003.
- ¹⁵ M. Joyeux, R. Schinke, and S. Yu. Grebenshchikov. *J. Chem. Phys.*, 120:7426, 2004.
- ¹⁶ T. P. Grozdanov, V. A. Mandelshtam, and H. S. Taylor. *J. Chem. Phys.*, 103:7990, 1995.
- ¹⁷ E. E. Nikitin. *Theory of Elementary Atomic and Molecular Processes in Gases*. Clarendon, Oxford, 1974.
- ¹⁸ V. N. Ostrovsky and H. Nakamura. *J. Phys. A*, 30:6939, 1997.
- ¹⁹ N. Yu. Demkov and V. N. Ostrovsky. *Phys. Rev. A*, 61:032705, 2000.
- ²⁰ H. Nakamura. *J. Chem. Phys.*, 87:4031, 1987.
- ²¹ A. Piryatinski, M. Stepanov, S. Tretiak, and V. Chernyak. *Phys. Rev. Lett.*, 95:223001, 2005.